Recent Developments in the ATLAS Pixel Detector

Francesco Ragusa [a,1]

[a] *Dipartimento di Fisica, Università di Milano and INFN, Sezione di Milano, via Celoria 16, I-20133 Milano, Italy*

Abstract

Silicon pixel detectors, developed to meet LHC requirements were tested in 1998 and 1999 within the Atlas collaboration in the H8 beam at CERN. Different sensor designs have been studied using an analog front end electronics chip. In this work a detailed experimental study of the overall performance of both irradiated and not irradiated detectors for the different designs is presented, with special emphasis to efficiency, charge collection and resolution measurements. Behavior of detectors in a magnetic field is also discussed.

1 Introduction

The ATLAS Pixel Detector [1] will be operated in a severe environment where a high efficiency has to be achieved despite the radiation damage and the challenging high data acquisition rate. To meet these requirements a special effort is in progress to develop radiation resistant sensors and front end electronics. Details of electronics and sensors designs are given elsewhere [1,2]; here we recall some basic aspects important to discuss the results presented here.

Front end electronics. To achieve high data acquisition rate with the high luminosity LHC machine the data of a pixel hit (address, pulse amplitude, bunch crossing number) selected by a Level 1 Trigger will be stored in the front end chip, operated synchronously with the 40 MHz machine R.F. Subsequently, if the event is selected by higher level triggers, the hit will be read-out from the front end chip local buffers using the stored bunch crossing number. The pulse height measurement is performed by measuring the time the pulse from the amplifier remains above the threshold (Time Over Threshold). During the operation in the test beam the thresholds of the individual channels were adjusted achieving a threshold dispersion of 170 electrons rms. Typical thresholds were around 3000 electrons, going down to 2000 electrons for charge collection studies. The noise

[1] On Behalf of the ATLAS Pixel Collaboration[1]

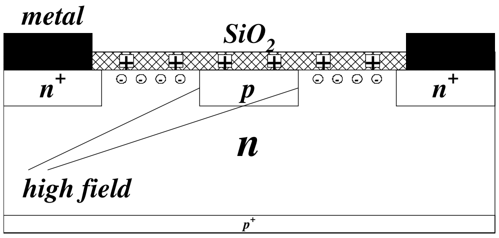

Fig. 1. Schematic view of the implants in the p-stop insulation method. The charges inside the square boxes are fixed, the charges inside circles are free.

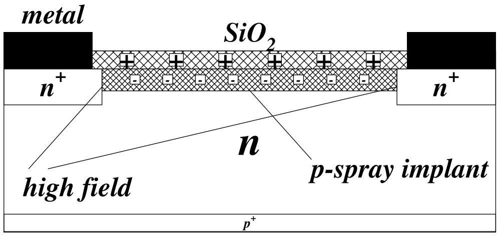

Fig. 2. Schematic view of the implants in the p-spray insulation method. The charges inside the square boxes are fixed.

was typically 150 electrons rms. The TOT was calibrated by injecting a known charge to every channel, with an accuracy of the order of 5 %.

Pixel detectors. A module of the ATLAS pixel detector consists of a *Tile* containing an array of 2×8 sensors. On each sensor, a front end electronic chip is bump bonded using Indium bumps or SnPb solders. The results reported in this paper are based on data collected with *single chip* assemblies made of one single sensor with a front end chip bump bonded on it. The pixel cells, 400 μm times 50 μm in size, were obtained by n^+ implants on *n-type* substrate; a well known problem with this kind of detectors is the presence of a low resistance layer of free electrons near the silicon/SiO_2 interface (due to presence of fixed positive charge in the oxide) which shorts two adjacent pixels. To achieve electrical insulation between pixels two different solutions were used: the so called *Tile 1* design (Fig. 1) in which the pixel cells were insulated using high dose *p-stop* implants [2,3] surrounding the pixel cells and the *Tile 2* (Fig. 2) design in which the insulation was obtained by a uniform medium dose implant employing the *p-spray* technique [2,4]. With the p-stop method the electrons layer between two adjacent pixels is interrupted by the p implant while with the p-spray method the electrons are neutralized by the acceptors in the medium dose p implant. These two techniques have different radiation resistances: regions with high electric field are present at the interface of the p implants (Fig. 1 and Fig. 2); the field intensity is function of the positive charge density in the SiO_2 and, if the fields become too strong, breakdown can occur and the detector cannot be operated anymore. The exposure to high fluxes of charged particles increases the density of fixed positive charges in the SiO_2; however the field at the interface increases for the p-stop scheme while it decreases for the p-spray scheme. This is in agreement with our observation of a better radiation resistance of the sensors using the p-spray insulation. The p-stop and the p-spray techniques have been carefully studied in ref. [4]. Several sensors designs have been realized and tested. In this paper we report measurements on three designs:

- *design a*, 280 μm thick, using p-stop insulation in the form of a p implant surrounding every pixel cell;
- *design b*, 280 μm thick, using p-spray insulation; the pixels are surrounded by a floating atoll (Fig. 3) to reduce the interpixel capacitance; during operation the floating atoll should be charged by the dark current and reaches an equilibrium field configuration in which the ionization electrons are focused on the pixel;
- *design c*, 200 μm thick, using p-spray insulation; similar to design b but without the floating atoll (Fig. 4).

Design b and design c also feature a *bias grid*, used to bias all the pixels by the *punch through mechanism*; this feature is used to test the sensors before bump bonding to front end chips; during normal operation the grid is not used and the bias to the pixels is given by the connected preamplifiers. As will be shown in sections 2 and 3 the design b had a charge collection problem related to the presence of the floating atoll surrounding the pixel; for this reason design c was developed.

To asses the radiation resistance of the sensor, some detectors were exposed to a flux comparable to those expected for LHC. Irradiations were performed using the 300 MeV/c pion beam at PSI and the 55 MeV/c proton beam at LBNL. In what follows the doses will be converted in

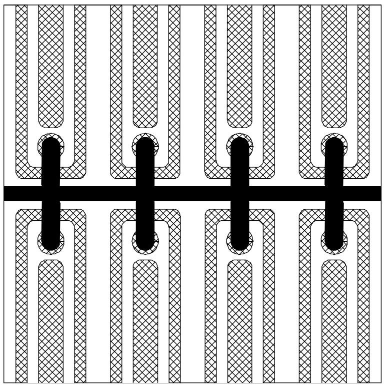

Fig. 3. Schematic view of the n implants and the bias grid for the design b. The hatched regions are the n implants while the black regions are the metal lines of the bias grid.

n_{eq}/cm^2 where n_{eq} is the number of particles with the non-ionizing energy loss of a 1 MeV neutron [5,6]. Sensors irradiated with fluences of 0.5×10^{15} and 1×10^{15} n_{eq}/cm^2 were tested, the last one corresponding approximately to 5 years of LHC operation for the first barrel layer and 10 years for the second barrel

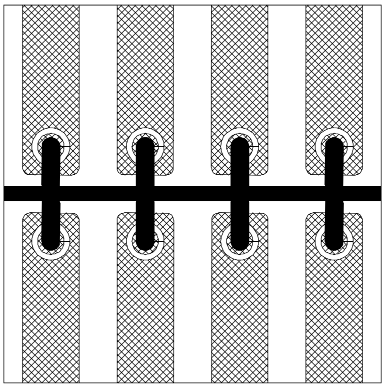

Fig. 4. Schematic view of the n implants and the bias grid for the design c. The hatched regions are the n implants while the black regions are the metal lines of the bias grid.

layer at 4.3 cm and 10.1 cm from the beam line respectively; the lifetimes calculations assume a linear increase of the luminosity for the first 3 years from 10^{33} cm^{-2}s^{-1} to the nominal design luminosity of 10^{34} cm^{-2}s^{-1}. The irradiated sensors were kept at -9^0 C during data taking.

Test beam setup. The studies presented in this paper were done at the CERN SPS accelerator with a pion beam of 180 GeV/c momentum. During the extraction, the beam lost his R.F. structure and the particles crossing the detector had a random phase with respect to the front end electronics 40 MHz clock: this phase was measured using a TDC started by the beam particle trigger (done using two scintillator/photomultiplier counters in coincidence) and stopped by the first falling edge of the clock. Further, for an accepted trigger of beam particle crossing the detector, up to 16 Level 1 triggers contiguous in time were sent to the front end chip and were subsequently read-out to simulate a sequence of 16 bunch crossings; this allowed to study the timing behavior of the detector. A beam telescope consisting of 4 pairs of silicon microstrip detectors with analog readout was used to measure the transverse position of the incident beam particles. Each pair consisted of 2 planes of detectors with orthogonal strips of 50 μm pitch. The resolution on the point of the trajectory extrapolated at the pixel detector varied from 4.5 μm to 6.0 μm , depending on the position of the detector under test with respect to the telescope.

2 Efficiency

Efficiency losses were studied originating either from the pixel sensor or from the analog part of the front end electronics. They are due either to a missing hit, because of a low pulse height below threshold, or to a large time walk that would cause the wrong assignment of the hit to a bunch crossing different from the expected one (from now on BX 0). To measure the efficiency, the intersection of the trajectory of a beam particle with the plane of the pixel detector was calculated; the number of expected hits was evaluated by requiring the extrapolated point to be at least 40 μm from the edges of the detector (to prevent the resolution of the telescope to bias the measurement of the efficiency). When a hit was expected, 4 classes were considered:

- no hit was found (*missing hits*);
- a hit was found near the extrapolated point in the expected bunch crossing (*good hits*);
- a hit was found near the extrapo-

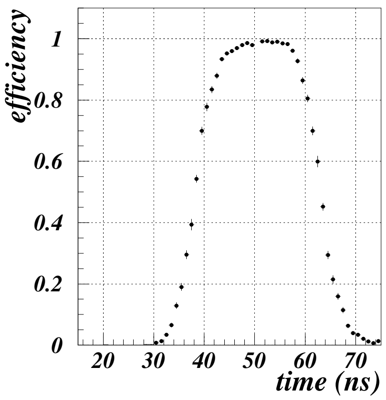

Fig. 5. Efficiency versus time for a sensor of the design b type.

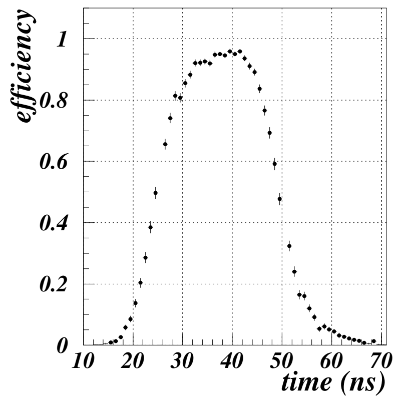

Fig. 6. Efficiency versus time for a sensor of the design b type after irradiation.

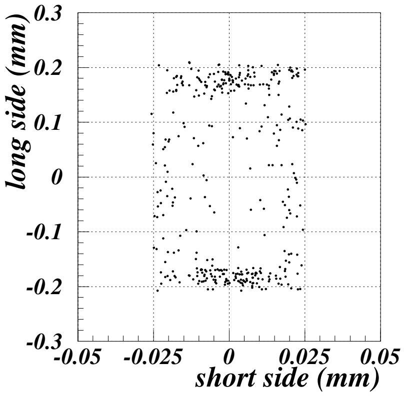

Fig. 7. Position of the missing hits for an irradiated design b type sensor.

lated point but not in the expected bunch crossing (*timing losses*);
- a hit was found far from the extrapolated point (*tracking losses*).

The *good hits* class was further classified depending on the number of adjacent hits. For each class the fraction with respect to the expected number of hits was calculated as a function of the beam particle phase. The efficiency as a function of the beam particle phase for BX -1, BX 0 and BX $+1$ is shown in Fig. 5 for a 280 μm thick design b type sensor; for convenience the data of the 3 bunch crossings were put on the same figure with the following convention: BX -1 from 0 to 25 ns, BX 0 from 26 to 50 ns and BX $+1$ from 51 to 75 ns. We observe a region of almost constant efficiency extending for about 9 ns from 48 ns to 56 ns. Similar plots for design a type sensors showed a flat region extending approximately 11 ns. The efficiency versus time for a design b type sensor after an irradiation equivalent to 10^{15} $\mathrm{n_{eq}/cm^2}$ is shown in Fig. 6; the region of constant efficiency is now reduced to approximately 5 ns. The classes introduced previously were studied in the time windows of almost flat efficiency described before; the results are shown in table 1. It was not possible to operate the design a type sensor after an irradiation equivalent to 10^{15} $\mathrm{n_{eq}/cm^2}$; although the design a sensor had efficiency performances superior to the design b it did not survive the radiation damage foreseen for the LHC environment. For a deeper understanding we studied the position dependence of the losses; as an example, Fig. 7 shows the position of the missing hits with respect

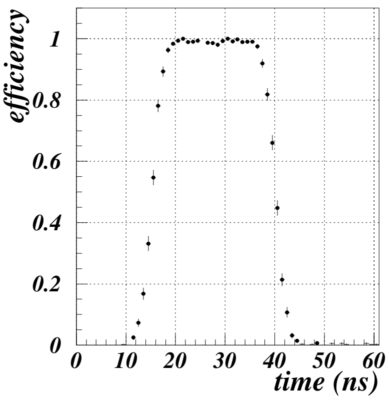

Fig. 8. Efficiency versus time for a sensor of the design c type.

to the center of the pixel cells for an irradiated sensor of the design b type: the losses are clearly localized at the edges of the pixel cells. Similar results were obtained studying the position of the timing losses. As will be shown in section 3 the design b had a charge collection inefficiency in the region of the floating atoll. The design c was realized to correct this problem removing the floating atoll and improving the bias grid geometry (Fig. 4); the new sensors were tested in a test beam in may 1999; the efficiency versus time for a 200 μm thick sensor of the design c type is shown in Fig. 8 and the detailed study of the efficiency in table 1. An efficiency better than 99 % was obtained with a flat top of 16 ns. Studies of the new design after radiation damage are in progress; however, to get an estimate of the efficiency for an irradiated p-spray design without the charge loss problem, a measurement of the efficiency for the design b sensor was done requiring that the beam particles crossed the pixel in a region within $\pm$ 10 μm and $\pm$ 150 μm from the center of the pixel cell along the short and the long dimension respectively. A flat top of approximately 9 ns and an efficiency of 98.4 % were obtained. The results are summarized in the last column of table 1.

3 Charge Collection

The ability of the front end electronics to measure the pulse height with the time over threshold technique gave the possibility to measure the charge collected by the pixels and to study it as a function of the impact point of traversing particles relative to the center of a pair of pixel cells. For hits not at the pixel center, the signal is shared between several pixels; the sum of the pixels pulse height (cluster pulse height) is calculated. During these measurements the electronics threshold was set at 2000 electrons. This threshold consequently reduced the amount of charge that could be measured in regions where it was collected by more than one pixel. The average cluster charge

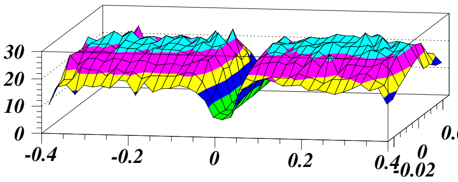

Fig. 9. Average cluster charge as a function of the transverse beam position for a design b type sensor.

as a function of positions x and y is shown in Fig. 9 where the coordinate axes are parallel to the short (50 μm) and long (400 μm) edges of the pixels, respectively, and are centered (in x) at the center of a single pixel and (in y) between two adjacent pixels. The average charge collected at the

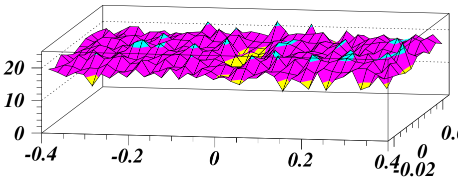

Fig. 10. Average cluster charge as a function of the transverse beam position for the design c type sensor.

center of the pixel was $28{\cdot}10^3$ electrons; regions with reduced charge collection were observed for the design b type sensors; these regions are located at the center of the plots in y or at the edges of the pixels in both x and y. A possible explanation [2] of this is that the n^+ implant ring that surrounds the main pixel implant (and which was introduced to minimize inter-pixel capacitance) did not float as it should, due to the presence of a current path not evident in the two-dimensional simulations used to optimize the design. It consequently collected signal charge of which part was then lost due to capacitive coupling to parasitic nodes (e.g. the bias grid). (A study using three-dimensional simulation is in progress to better understand this.) At the end of each pixel that is directly adjacent to the bias grid, two charge loss effects combine: the capacitive effect described above and a direct loss to the implanted bias dot. In this region a relatively large amount of charge loss is visible, extending approximately $\pm$ 50 μm into the pixel region in the y direction; this loss profile corresponds roughly to the geometry of the bias structure. As can be seen from Fig. 10 the first charge loss effect is absent from the design c sensors, which has no n^+ implant ring. Results for this design show only a small charge collection inefficiency at alternate gaps, corresponding to the presence of the bias grid, which includes an n^+ implantation line. Sensors of design a type show only a small charge collection inefficiency on all sides of each pixel. The small gap between the individual p-stop rings acts (due to electron

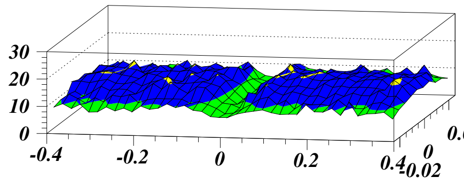

Fig. 11. Average cluster charge as function of the transverse beam position for a sensor of design b type after irradiation.

accumulation) like a small n^+ region [2]. Finally, in Fig. 11 the average cluster charge as a function of the beam particle position is shown for a design b type sensor irradiated with a fluence of 10^{15} n_{eq}/cm^2. The sensor (280 μm thick) was operated with a depletion potential of -600 V; as will be shown in section 5 under this bias condition the sensor was only partially depleted, the depletion depth being approximately 190 μm . The average charge collected at center of the pixel was $15{\cdot}10^3$ electrons and the charge losses at the edge of the pixel cells were similar to the not irradiated design b sensor.

4 Resolution

The spatial resolution was measured by computing the residuals between the hit position predicted by the silicon microstrip telescope and that from the pixel detector. Single pixel and double pixel clusters were studied separately; double pixel clusters were studied using two different algorithms: a *binary* algorithm, in which the measured cluster position was taken at the center of the 2 hit pixels and an *analog* algorithm in which

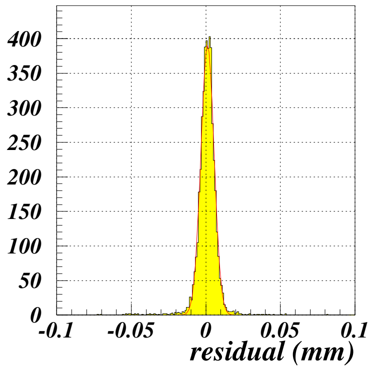

Fig. 12. Distribution of the residuals for the 2 pixels clusters using the analog algorithm.

the binary position was corrected using the measured charge collected by the 2 hit pixels. The charge sharing between 2 pixels was studied separately: for the 280 μm thick sensor of design b type, with a threshold of 3000 electrons, the region of charge sharing was limited to approximately $\pm$ 6 μm around the center of the 2 pixel cells; this region was reduced to approximately $\pm$ 4 μm for the design c 200 μm thick sensors. The distribution of the residuals of a design c 200 μm thick sensor for the analog and binary algorithm is shown in Fig. 12 and Fig. 13 respectively. For these measurements, the error on the

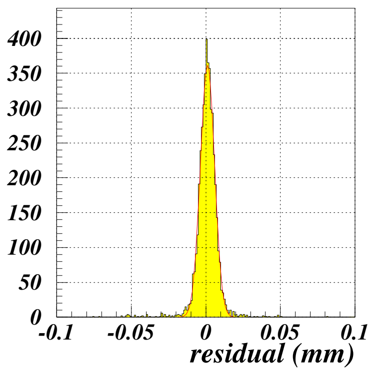

Fig. 13. Distribution of the residuals for the 2 pixels clusters using the binary algorithm.

predicted hit position was 4.2 μm , calculated taking into account the resolution of the silicon microstrip planes and the multiple scattering due to material of the experimental setup. The width of the residuals was calculated fitting the distributions with a Gaussian function and gave 4.4 μm and 4.8 μm for the analog and digital algorithm respectively. The single pixel cluster residual distribution is shown in Fig. 14. The

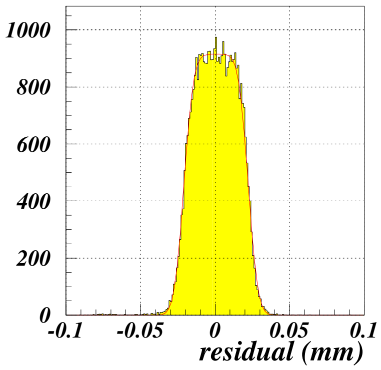

Fig. 14. Distribution of the residuals for the 1 pixel clusters.

distribution was parametrized with a uniform distribution of width L, as expected for the single pixel cluster residuals, convoluted with a Gaussian distribution that took into account the resolution of the silicon strip telescope. The result of the fit gave σ = 5.2 $\pm$ .1 μm and L = 43.2 $\pm$ 0.2 μm; the fitted width L is in agreement with the measured width of $\pm$ 4 μm of the region in which charge sharing occurs. The single pixel and double pixel cluster residual were put together and the resulting distribution is shown in Fig. 15. The rms of the distribution was 13.4 μm; subtracting the resolution of the silicon telescope a value of 12.7 μm was obtained that is a measurement

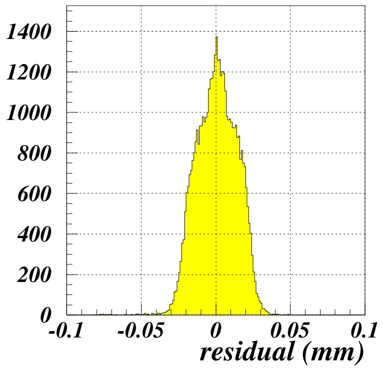

Fig. 15. Distribution of the residuals for the 1 pixel clusters and 2 pixels clusters using the binary algorithm.

of the resolution of the sensor for normal incidence of the beam particles. The relative weight of the single pixel and double pixels clusters can be seen from table 1 were the fraction of double hits is given. Finally, the dependence of the resolution on the angle of the incident particle was studied. For each angle of incidence of the track, the rms of the residuals distribution (single and double pixel cluster) was measured using the binary and the analog algorithm. The results are shown in Fig. 16 where the rms of the residuals measured with a sensor irradiated at a fluence of 10^{15} n_{eq}/cm^2 is also plotted. The data were not corrected for the

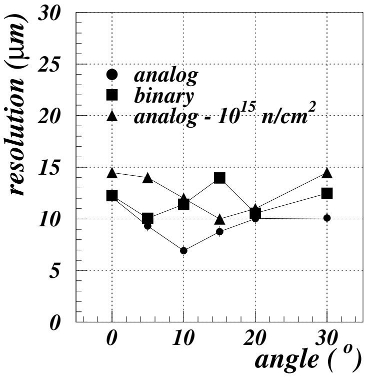

Fig. 16. Width (rms) of the residuals versus the track incidence angle.

silicon strip telescope resolution. It can be noticed that at an angle of 10^0 the analog algorithm allows to obtain a resolution better than 6 μm . This improvement was due to the increased cluster size and thus increased charge sharing between neighboring pixels. The irradiated detector resolution never reaches values below 10 μm because of the small fraction of double pixel cluster (7.6 %). However it should be noticed that this is a sensor of design b type, suffering the charge collection problems discussed in section 3, and an improvement is expected with the new design c sensors.

5 Depleted depth

The choice of the n^+/n technology has the consequence that during the operation in the LHC environment the silicon bulk material will undergo a *type inversion* becoming of *p type*. The variation of the effective doping and the increase of the leakage current will eventually prevent the fully depleted operation of the detector. The depletion depths of two design b type sensors, irradiated with a fluence of 0.5×10^{15} and 10^{15} n_{eq}/cm^2 respectively, were measured. To measure the depletion depth data were taken with the sensor at an angle of 30^0 with respect to the direction of the beam along the short direction of the pixel cells. The method is illustrated in Fig. 17: a beam particle crossing the detector produced a cluster consisting of the pixel cells which collected the charge of the

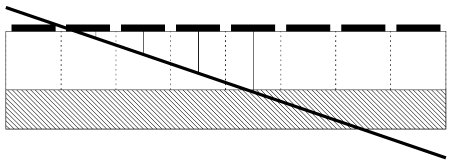

Fig. 17. Illustration of the measurement of the depletion depth.

subtended segment of the track; for each segment the depth of the center of the segment was calculated. The distribution of the depths is shown in Fig. 18; the peak at low depth is due to the definition of depth for the first pixel that is different since part of the track is outside the detector. From the figure the maximum depth at which the charge was still collected can be measured: to fit the rightmost part of the distribution of the depth d the function $f(d) = a(1 - \tanh b(d - d_{max}))$ was used where a was a normalization factor, b a width parameter, and d_{max} the maximum depth. From the fit we obtained $d_{max} = 190 \pm 14$ μm for the sensor irradiated at a fluence of 10^{15} $\mathrm{n_{eq}/cm^2}$ and $d_{max} = 265 \pm 11$ μm for the sensor irradiated with 0.5×10^{15} $\mathrm{n_{eq}/cm^2}$. Both detectors were 280 μm thick and were biased at -600 V. It can be noticed that the p-spray sensors are almost fully depleted after a dose of 0.5×10^{15} $\mathrm{n_{eq}/cm^2}$ when biased at -600 V.

6 The Lorentz angle

The ATLAS pixel detector will operate in a magnetic field of 2 Tesla; in the barrel part of the detector,

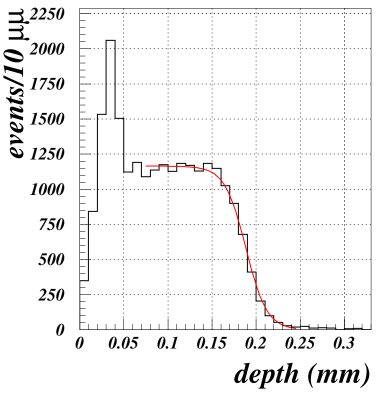

Fig. 18. Distribution of the depth of the charge segments for an irradiated sensor.

the magnetic field $\vec{B}$ and the electric drift field $\vec{E}$ inside the silicon pixel detector will be orthogonal and the drift velocity will acquire a component along the direction of $\vec{E} \times \vec{B}$; the charge carrier will then drift at an angle θ_L with respect to the direction of the electric field, θ_L being the Lorentz angle[7]. Depending on the angle of the incident particle, the charge collected will spread over several pixel cells, the spread being minimum for an angle of the incident particle equal to θ_L. The Lorentz angle for irradiated and not irradiated detectors of the design b type was measured. The method used is well known [8]: the mean cluster size was measured as a function of the angle of the incident beam particles with respect to the normal to the detector. For each angle 2 measurements were performed with magnetic field off, $\vec{B} = 0$, and magnetic field on $\vec{B} = 1.4$ Tesla. The mean cluster size as a function of the angle for a not irradiated detector operated at a bias voltage of -150 V is shown in Fig. 19; a fit to data is also shown. The fitting function was constructed using a

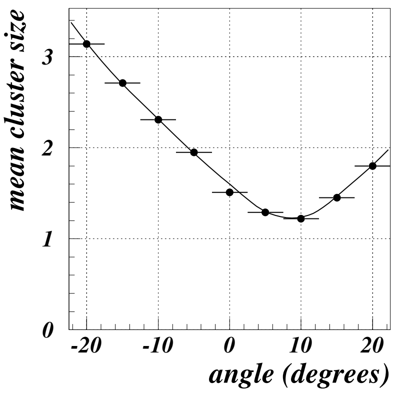

Fig. 19. Mean cluster size as function of the beam angle for a detector before irradiation.

simple model in which the ionization charge produced along the particle track was divided in small segments and each segment was propagated towards the pixel cells taking into account the Lorentz angle and the diffusion. Once all the charge was collected by the pixel cells, a threshold was applied and the cluster size was evaluated. This procedure was repeated for different positions of the incident beam particle with respect to the pixel cells. The mean cluster size was then evaluated. The model described did not take into account yet the Landau fluctuations. The fit was performed both on the magnetic field on and magnetic field off data. With magnetic field off the Lorentz angle should be zero and a result different from zero was taken as systematic error for the fit with magnetic field on. The results obtained were $\theta_L = 9.1^0 \pm 0.1^0 \pm 0.6^0$ for a not irradiated sensor operated at -150 V, $\theta_L = 3.0^0 \pm 0.5^0 \pm 0.2^0$ for a sensor irradiated with 0.5×10^{15} $\mathrm{n_{eq}/cm^2}$ and operated at -600 V and $\theta_L = 3.2^0 \pm 1.2^0 \pm 0.5^0$ for a sensor irradiated with 10^{15} $\mathrm{n_{eq}/cm^2}$ and operated at -600 V, where the first error is statistical and the second one systematic.

7 Conclusions

A big effort was undertaken within the ATLAS Collaboration to finalize the pixel detector project. Sensors with different designs and different insulation techniques were studied in a test beam and detailed studies of the efficiency were presented and discussed. The *p-spray* insulation technique was proven to be radiation resistant and efficiencies exceeding 99 % with time plateau of 16 ns were measured. The p-spray design b sensors had a charge collection inefficiency due to a floating atoll that did not float as it should, due to the presence of a current path not evident in the two-dimensional simulations used to optimize the design; a new p-spray design(design c) was developed that removed the charge collection inefficiency. The charge sharing between adjacent pixel cells was studied and found to be confined within ±4 μm and ±6 μm around the center of the 2 pixels for 200 μm and 280 μm thick sensors respectively. Binary and analog algorithms for the coordinate measurement were studied and the resolution as a function of the incident angle of the track measured: a resolution better than 6 μm was measured at an angle of incidence of 10^0. The depleted depth of a 280 μm thick detector of design b type, irradiated with a fluence of 10^{15} $\mathrm{n_{eq}/cm^2}$, was measured to be 190 $\pm$

14 μm with a bias voltage of -600 V. The Lorentz angle in a field of 1.4 Tesla varied from $\theta_L = 9.1^0 \pm 0.1^0 \pm 0.6^0$ for a not irradiated sensor operated at -150 V to $\theta_L = 3.2^0 \pm 1.2^0 \pm 0.5^0$ for a sensor irradiated with 10^{15} $\mathrm{n_{eq}/cm^2}$ and operated at -600 V and at a temperature of -9^0 C.

8 Acknowledgements

The work reported here represents the joint efforts of many individuals in the ATLAS Pixel Collaboration. I would like to thank all of them.

References

[1] The ATLAS Pixel Collaboration, ATLAS Pixel Detector Technical Design Report, LHCC 98/13, CERN 1998.

[2] The ATLAS Pixel Collaboration, "The ATLAS Silicon Pixel Sensors", Nucl. Instr. and Meth., submitted for publication.

[3] G. Batignani et al., Nucl. Instr. and Meth. A 277 (1989) 147.

[4] R.H. Richter et al., Nucl. Instr. and Meth. A 377 (1996) 412.

[5] R. Wunstorf, IEEE Trans. on Nucl. Sci. 44(3) (1997) 806.

[6] H. Feick, "Radiation Tolerance of Silicon Particle Detectors for H.E. Physics Experiments", Ph. D. thesis University Hamburg and DESY internal report F35D 97 08 (1997).

[7] S.R. Amendolia et al., Nucl. Instr. and Meth. A 235 (1985) 296.

[8] N. Bingefors et al., Nucl. Instr. and Meth. A 328 (1993) 447.

Table 1
Efficiency measurement summary.

Fluence (n/cm^2)	0	0	0	10^{15}	10^{15}
Design	b	a	c	b	b^*
1 hit	82.0	72.0	81.8	86.3	94.2
2 hits	14.6	25.2	15.6	7.6	3.1
$\geq$ 3 hits	2.2	2.4	1.7	1.4	1.1
efficiency	98.8	99.6	99.1	95.3	98.4
losses	1.2	0.4	0.9	4.7	1.6
0 hits	0.4	0.1	0.4	2.2	0.4
tracking	0.2	0.2	0.1	0.1	0.0
timing	0.6	0.1	0.4	2.4	1.2

* with position cut, see text